tvst

https://doi.org/10.1167/tvst.7.5.4

Article

Imaging Melanin Distribution in the Zebrafish Retina Using Photothermal Optical Coherence Tomography

Maryse Lapierre-Landry[1,2], Alison L. Huckenpahler[3], Brian A. Link[3], Ross F. Collery[3,4], Joseph Carroll[3,4], and Melissa C. Skala[2,5]

[1] Biomedical Engineering, Vanderbilt University, Nashville, TN, USA
[2] Morgridge Institute for Research, Madison, WI, USA
[3] Cell Biology, Neurobiology & Anatomy, Medical College of Wisconsin, Milwaukee, WI, USA
[4] Ophthalmology & Visual Sciences, Medical College of Wisconsin, Milwaukee, WI, USA
[5] Biomedical Engineering, University of Wisconsin Madison, Madison, WI, USA

Correspondence: Joseph Carroll, Department of Ophthalmology & Visual Sciences, Medical College of Wisconsin, 925 North 87th St, Milwaukee, WI 53226-0509, USA. e-mail: jcarroll@mcw.edu
Melissa C. Skala, Morgridge Institute for Research, 330 North Orchard St, Madison, WI 53715, USA. e-mail: mcskala@wisc.edu

Received: 17 May 2018
Accepted: 31 July 2018
Published: 4 September 2018

Keywords: optical coherence tomography; retinal pigment epithelium; melanin; zebrafish

Citation: Lapierre-Landry M, Huckenpahler AL, Link BA, Collery RF, Carroll J, Skala MC. Imaging melanin distribution in the zebrafish retina using photothermal optical coherence tomography. Trans Vis Sci Tech. 2018;7(5):4, https://doi.org/10.1167/tvst.7.5.4

Purpose: To demonstrate and validate that photothermal optical coherence tomography (PT-OCT) can image melanin in the retinal pigment epithelium (RPE) and can observe light-driven melanosome translocation in the zebrafish retina.

Methods: A commercial spectral domain OCT system was modified to perform both OCT and PT-OCT. Four adult tyrosinase-mosaic zebrafish with varying levels of melanin expression across their retinas were imaged, and the PT-OCT signal for pigmented and nonpigmented regions were compared. Wild-type dark-adapted ($n = 11$ fish) and light-adapted ($n = 10$ fish) zebrafish were also imaged with OCT and PT-OCT. Longitudinal reflectivity and absorption profiles were generated from B-scans to compare the melanin distribution between the two groups.

Results: A significant increase in PT-OCT signal ($P < 0.0001$, Student's *t*-test) was observed in pigmented regions of interest (ROI) compared to nonpigmented ROIs in the tyrosinase-mosaic zebrafish, which confirms the PT-OCT signal is specific to melanin in the eye. A significant increase in PT-OCT signal intensity ($P < 0.0001$, Student's *t*-test) was also detected in the light-adapted wild-type zebrafish group compared to the dark-adapted group. Additionally, light-adapted zebrafish display more distinct melanin banding patterns than do dark-adapted zebrafish in PT-OCT B-scans.

Conclusions: PT-OCT can detect different levels of melanin absorption and characterize pigment distribution in the zebrafish retina, including intracellular changes due to light-driven melanosome translocation within the RPE.

Translational Relevance: PT-OCT could quantify changes in pigmentation that occur in retinal diseases. The functional information provided by PT-OCT may also enable a better understanding of the anatomical features within conventional OCT images.

Introduction

Optical coherence tomography (OCT) is a standard imaging technique that provides high-resolution, depth-resolved images of different tissue layers without the need for contrast agents. It is used in both clinical and research settings to noninvasively detect, monitor, and study multiple eye conditions in vivo, either in patients or animal models.[1] As OCT becomes more widely used to monitor retinal diseases, it is important to correctly identify the anatomical features that correspond to OCT image features for the human retina and multiple animal models.[2] Previous efforts to label OCT image features have relied on comparisons to histology.[2–4] However, the relative thickness and appearance of retinal layers is not always conserved between histology and OCT images, which complicates the labeling process.[2] Additionally, the main source of contrast in OCT is tissue backscattering, a property that cannot be

directly compared to cell morphology in fixed samples. As a result, there is still controversy regarding the proper labeling of some retinal structures on OCT scans, particularly the bands associated with the photoreceptors and retinal pigment epithelium (RPE).[4,5]

One of the major scattering sources in the retina is melanin, which is located in the RPE and choroid. Retinal melanin varies with age and between individuals, and pigmentation changes are also associated with diseases such as age-related macular degeneration (AMD)[6] and retinitis pigmentosa.[7] In AMD, hyperpigmentation which may be due to RPE cell dysfunction, followed by hypopigmentation due to RPE cell loss is observed in geographic atrophy. These pigmentation changes in the RPE are thought to happen before dysfunction and death of the photoreceptors and thus could be predictive of disease progression.[6,8] Melanin is a major contributor to the appearance of the OCT RPE band and by extension the surrounding bands corresponding to the photoreceptors and Bruch's membrane.[9,10] An independent, validated method to image the melanin would allow researchers to quantify changes in pigmentation in the RPE and better understand how melanin affects OCT images, which could lead to a better understanding of diseases for researchers and better diagnosis and monitoring tools for clinicians.

Multiple imaging techniques have been developed to detect retinal melanin. Near-infrared autofluorescence (excitation at 787 nm) can be used to detect melanin in the RPE and choroid but is limited to two-dimensional (2D) en face imaging, and quantifying melanin in these images is not currently possible.[11–13] Photoacoustic microscopy (PAM) has also been used to image and quantify the distribution of melanin in the RPE and choroid.[14] Due to its low axial resolution PAM has mostly been used to create 2D en face images, but recent improvements have been made to distinguish the RPE from the choroid and produce depth-resolved images.[15] Functional OCT techniques such as polarization-sensitive (PS-OCT)[16] and photothermal OCT (PT-OCT)[17,18] have also been used to detect retinal melanin. Since they are based on the OCT signal, both modalities can produce 3D images of the retinal melanin distribution with axial and transverse resolution similar to OCT. Additionally, these images of melanin distribution are automatically coregistered to corresponding OCT intensity images showing retinal morphology. However, PS-OCT and PT-OCT use different contrast mechanisms. PS-OCT measures the depolarization of backscattered light and has been used to detect the presence of melanin in patients[19] and animal models[20] and to segment to RPE.[21] However, the degree of polarization uniformity measured with PS-OCT depends on the scattering properties of the sample, especially the size and shape of pigment granules, and does not decrease uniformly with respect to melanin concentration, especially at high melanin concentrations.[22] This limits the ability of PS-OCT for quantitative measurements. Alternatively, PT-OCT detects melanin based on its absorption coefficient. PT-OCT could be used to directly image and quantify retinal melanin to disambiguate the OCT signal in regions of the retina such as the RPE where melanin is present.

PT-OCT is performed by combining an amplitude-modulated laser to an OCT system, where the wavelength of this additional laser corresponds to a region of high absorption for the contrast agent (e.g., melanin). The absorbed light creates a small increase in temperature around the contrast agent, which causes a local expansion of the tissue and a change in the refractive index. Both effects cause a change in optical path length, which is detected as a change in phase of the OCT signal at the same frequency as the amplitude-modulation frequency of the laser. The PT-OCT signal is then computed during postprocessing and shows the location of the contrast agent in the OCT field of view. In previous studies, PT-OCT has been demonstrated in vitro,[18] ex vivo,[23] and in vivo[24] using exogenous contrast agents such as gold nanoparticles[25] or indocyanine green.[26] More recently, PT-OCT of melanin has been demonstrated in vivo in skin[27] and in the mouse eye.[28] The PT-OCT signal is linearly proportional to the absorption coefficient of a sample and can thus be used to evaluate relative concentrations of a contrast agent.[24]

In this study, PT-OCT was used to image the zebrafish eye, to our knowledge for the first time. Zebrafish have a cone-rich retina that can be imaged with OCT.[10,29,30] Many genetically modified lines are also available.[31] Genetically modified zebrafish in which pigment synthesis is disrupted resulting in cells either expressing or not expressing melanin (tyrosinase-mosaic)[10] were used to image variations in pigmentation within the same eye. Additionally, melanosome translocation within the RPE cells due to light or dark adaptation is a well-known phenomenon in wild-type (WT) zebrafish.[32] This specific and highly repeatable perturbation was used to image subcellular changes in pigment distribution. In summary, we demonstrate that the PT-OCT signal

is specific to melanin and sensitive to different pigmentation levels and distribution in the zebrafish retina.

Methods

Instrumentation and Signal Analysis

A commercial spectral domain OCT system (Envisu R-2200, $\lambda = 860$ nm, 93-nm bandwidth, 36-kHz acquisition rate; Bioptigen, Durham, NC) was modified to perform PT-OCT imaging. A diode laser ($\lambda = 685$ nm; Coherent Inc., Santa Clara, CA) was added to the light path to provide photothermal excitation using a 50:50 fiber coupler. The diode laser was amplitude modulated internally following a square wave of frequency $f_0 = 500$ Hz, 50% duty cycle. From the 50:50 coupler, the light was directed into the reference and sample arm. A wideband optical circulator (AC Photonics, Santa Clara, CA) was used to send the backscattered light to a spectrometer and 2048 pixels CCD. The OCT light source originally had a power of 0.7 mW at the sample, but after the addition of the circulator, the power at the sample was reduced to 0.47 mW. The peak power of the photothermal laser was varied between 0 and 4.3 mW at the sample, depending on the experiment. A mouse retina lens (Bioptigen) was used to focus the light onto the zebrafish retina. Data were acquired using software (InVivoVue 2.4; Bioptigen). Each PT-OCT A-scan was composed of 700 repeated scans over time (M-scan), with 400 A-scans per B-scan. A PT-OCT B-scan took approximately 7 seconds to acquire. OCT volume scans and OCT line scans were also acquired for each eye. OCT volume scans were nominally 1.2×1.2 mm (500 A-scans/B-scans, 500 B-scans), and OCT line scans were nominally 1.2 mm (400 A-scans/B-scan, 50 averaged B-scans). Both scan types were scaled according to the protocol in Huckenpahler et al.[29]

Image analysis was performed following data collection using a custom MATLAB code previously described in Tucker-Schwartz et al.[24] The raw data was first resampled from wavelength to wavenumber, dispersion corrected,[33] and background subtracted. A Chirp-Z transform was then used to obtain the OCT magnitude and the phase signal as a function of depth. The time derivative of the phase signal over 700 M-scans was then taken at each depth, and a Fourier transform was performed to transition the phase signal from the time domain to the frequency domain. The PT-OCT peak signal is defined as the magnitude of the Fourier transformed phase signal at $f_0 = 500$ Hz, which is the photothermal laser modulation frequency. The PT-OCT noise signal is defined as the average signal from 250 to 400 Hz and 600 to 750 Hz. The PT-OCT signal is taken to be the noise signal subtracted from the peak signal and is expressed in units of nanometers of optical path length change due to the increased temperature.

Zebrafish

Zebrafish studies were approved by the Institutional Animal Care and Use Committee at the Medical College of Wisconsin and conducted in accordance with the ARVO Statement for the Use of Animals in Ophthalmic and Vision Research. One-year-old adult WT and tyrosinase-mosaic zebrafish were used in this study. Tyrosinase-mosaic fish were created by injecting WT zebrafish embryos with CRISPR/Cas9 reagents targeting the *tyr* locus to cause mosaic gene inactivation and disruption of melanin synthesis as described in Wilk et al.[10] To determine if the PT-OCT signal is specific to melanin and observe how the PT-OCT signal changes as a function of the photothermal laser power, four mosaic zebrafish were imaged with OCT and PT-OCT while under anesthesia (Tricaine), using photothermal laser powers of 0, 1.8, 2.6, and 4.3 mW. To study the melanosome translocation due to light, two WT light-adapted and two WT dark-adapted fish were first imaged as preliminary data. This experiment was then repeated with $n = 10$ light-adapted zebrafish and $n = 11$ dark-adapted zebrafish. The light-adapted fish were exposed to normal ambient light starting at 7 AM and imaged 4 hours later. Dark-adapted fish were protected from light overnight until the following day, when they were imaged in a dark room.

En face OCT images of the RPE were created by segmenting the RPE layer and averaging the OCT signal following an algorithm described in Huckenpahler et al.[29] OCT B-scans were created by averaging the OCT intensity signal from each PT-OCT B-scan (700 repeated A-scans at each pixel). Longitudinal reflectivity profiles (LRPs) were created by averaging the OCT signal using MATLAB over 20 to 400 neighboring A-scans. Similarly, longitudinal absorption profiles (LAP) were created for the same regions by averaging the PT-OCT signal over neighboring A-scans. A median filter was used to reduce the noise of the OCT and PT-OCT images before creating the longitudinal profiles. In the case of the LRP and LAP created by averaging 400 A-scans,

an image registration algorithm[34] was also used to align the retina over the entire B-scan before creating the longitudinal profiles.

Histology

The zebrafish were decapitated immediately after imaging while still under anesthesia and after gill movement had stopped. The heads were fixed in 4% paraformaldehyde overnight. Light- and dark-adapted zebrafish had the eyes dissected from the head and embedded in paraffin for hematoxylin and eosin (H&E) histology. Tyrosinase-mosaic zebrafish had the eyes dissected from the head and the anterior segment removed prior to imaging the scleral aspect of the intact eyecup as in Wilk et al.[10]

Statistical Analysis

Statistical comparisons were done using statistical software (Prism; GraphPad, La Jolla, CA). In all cases, an *F*-test was used to determine if the variances of two experimental groups were equal. A 2-tailed, Student's *t*-test with unequal variance was used to compare the PT-OCT signal from pigmented and nonpigmented regions of interest (ROIs) of the retina in mosaic zebrafish. Linear fits were also performed to determine if the PT-OCT signal in a given ROI was increasing linearly as a function of photothermal laser power. The origin $y = 0$ was fixed for each fit since no PT-OCT signal should be detected when the photothermal laser is off (0 mW). Three criteria were used to determine the quality of the fit and if the PT-OCT signal was proportional to laser power: the slope, the coefficient of determination, and the sum of squared errors. First, fits with a slope smaller than −0.1 were rejected since a positive relationship is predicted by theory.[24] Second, the coefficient of determination R^2 and the sum of squared residuals (SSR) were obtained as followed:

$$SSR = \sum_i (y_i - f_i)^2 \quad (1)$$

$$R^2 = 1 - \frac{SSR}{\sum_i (y_i - \bar{y})^2} \quad (2)$$

Where y_i are the experimental PT-OCT values, f_i are the values predicted by the linear fit, and $\bar{y}$ is the mean experimental value. As seen in Equation 2, R^2 is not an appropriate measure of the quality of the fit in cases where the PT-OCT signal remains zero as the power increases, which is expected if no pigment is present in the ROI ($y_i - \bar{y} \approx 0$). For this reason, the quality of the fit was determined to be acceptable if $R^2 > 0.5$, or SSR < 1 in cases where $R^2 < 0.5$.

In the second part of this study, a two-tailed Student's *t*-test with equal variance was used to compare the average PT-OCT signal from dark-adapted fish ($n = 11$) and light-adapted fish ($n = 10$). A Student's *t*-test with equal variance was also used to compare the power spectrum amplitude of the dark-adapted and light-adapted zebrafish at two spatial frequencies ($1/\Delta x_1 = 1/23.6$ μm, $1/\Delta x_2 = 1/11.8$ μm).

Results

PT-OCT Signal in the RPE Is Specific to Melanin

OCT and PT-OCT scans were acquired in all tyrosinase-mosaic fish. Pigmented and nonpigmented regions were identified based on the en face OCT image of the RPE, where pigmented regions had a higher OCT signal intensity compared to nonpigmented regions, as demonstrated in Wilk et al.[10] An example en face OCT image can be seen in Figure 1A. To confirm the location of the pigmented and nonpigmented regions, the en face OCT image was compared to an ex vivo posterior view of the eyecup (Fig. 1B), which shows identical pigmentation patterns. Two example B-scans from the same eye can be seen in Figure 1C where the PT-OCT signal has been overlaid onto the OCT signal. In this case, both PT-OCT B-scans were acquired using 2.85 mW of photothermal laser power. The PT-OCT signal is localized to the band corresponding to the RPE and is only present in pigmented sections of the retina (Figs. 1A, 1C, orange lines). No PT-OCT signal is detected in nonpigmented regions (black lines, Figs. 1A, 1C) or regions of the retina below the blood vessels (red circles, Fig. 1C). For all eyes ($n = 4$ eyes from four fish), B-scans acquired using 4.3 mW of photothermal laser power were divided in ROIs consisting of 10 neighboring A-scans. The average PT-OCT intensity was calculated for each ROI, and the ROI was classified as "pigmented" or "nonpigmented" based on the OCT en face and OCT B-scan images. Blood vessels degrade the OCT phase signal, resulting in poor signal-to-noise ratio (<1) and poor phase stability. Blood vessels can be identified based on morphology in OCT B-scans and en face views and as regions of negative PT-OCT signal (<−1 nm) in PT-OCT B-scans. No PT-OCT signal can be reliably detected from regions below blood vessels since noise

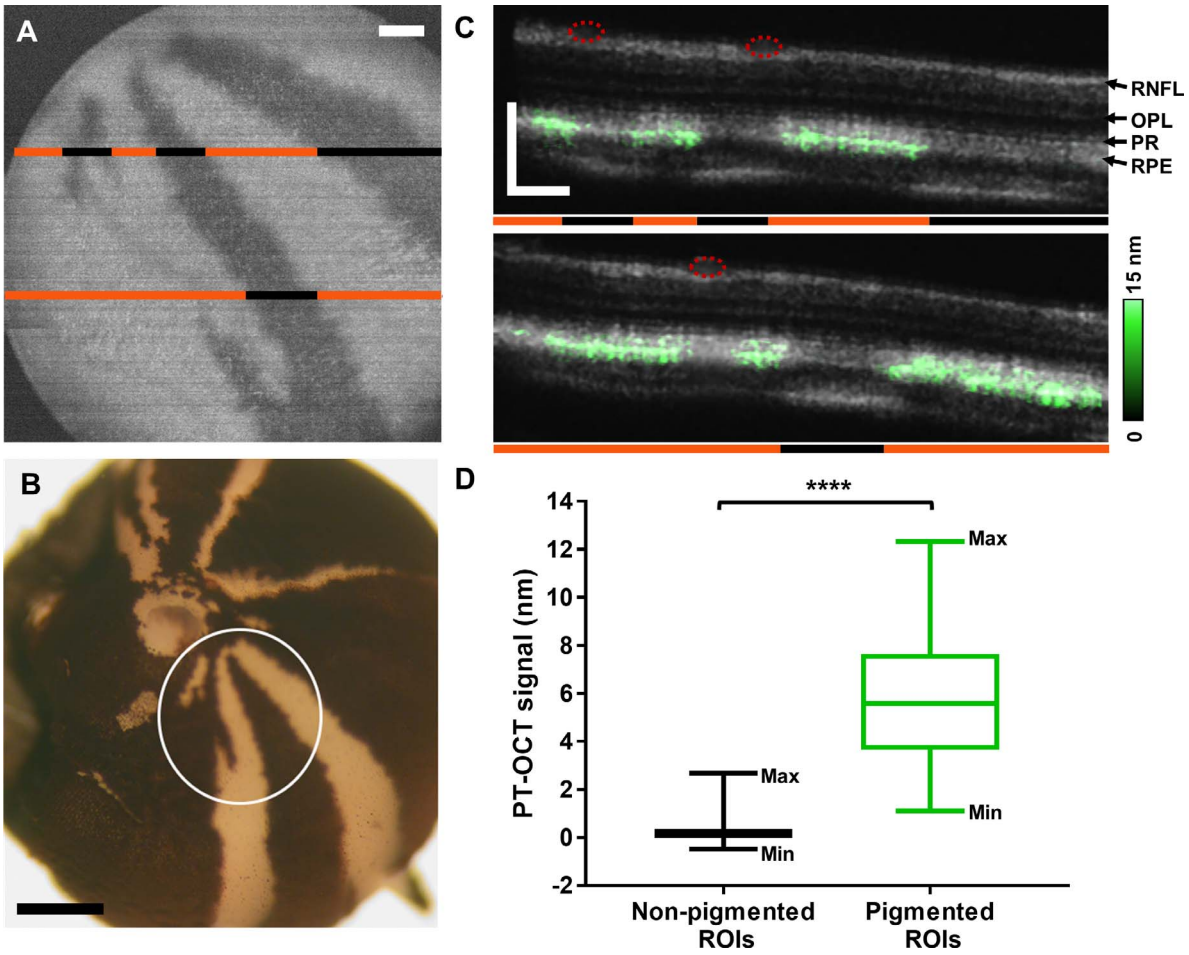

Figure 1. PT-OCT of melanin in tyrosinase-mosaic zebrafish. (A) En face OCT image of the RPE showing the pigmentation pattern. Areas of pigment are hyperreflective (*white*) while nonpigmented areas are hyporeflective (*dark*). (B) Posterior view of the eyecup. *White circle* indicates field of view shown in (A) where areas of pigment are *dark* and nonpigmented areas are *white*. (C) OCT (*gray*) and PT-OCT (*green*, overlaid) B-scans of the retina. The locations of the B-scans are indicated by the lines in (A). *Orange lines* denote pigmented areas and *black lines* denote nonpigmented areas. *Red circles* indicate presence of blood vessels. (D) Average PT-OCT signal for all nonpigmented and pigmented ROIs across $n = 4$ eyes from four zebrafish. Each ROI is 10 A-scans wide. Whiskers on the box plot show minimum and maximum values for each distribution. ****$P < 0.0001$ Student's *t*-test. RNFL, retinal nerve fiber layer; OPL, outer plexiform layer; PR, photoreceptors. *Scale bar*: 100 μm for OCT and 500 μm for histology.

dominates over signal. ROIs below blood vessels were thus not included in this analysis. As seen in Figure 1D, the PT-OCT signal in pigmented ROIs is significantly higher than for nonpigmented ROIs across all eyes ($P < 0.0001$, Student's *t*-test, $n = 53$ nonpigmented and $n = 150$ pigmented ROIs). The nonpigmented ROIs have an average signal of 0.23 ± 0.53 nm (mean ± standard deviation), while the pigmented ROIs have an average signal of 5.71 ± 2.50 nm. This significant increase in signal intensity demonstrates that PT-OCT is sensitive and specific to melanin expression in the zebrafish eye.

The distribution of PT-OCT signal in the pigmented ROIs has a high standard deviation (2.50 nm) that does not match the phase stability of our system (<1 nm). We hypothesize that the high variance in the PT-OCT signal over all pigmented ROIs is not the result of a high uncertainty on the measurements, but likely is a large range of absorption coefficients throughout the retina. Previous studies have confirmed that the PT-OCT signal is linearly proportional to the photothermal laser power and the local absorption coefficient of the sample.[24] Two perpendicular B-scans were thus acquired in each tyrosinase-mosaic eye at multiple photothermal laser powers to verify this linearity. As seen in Figure 2A, no PT-OCT signal is detected when the photothermal laser is off. However, a PT-OCT signal can be seen when the photothermal

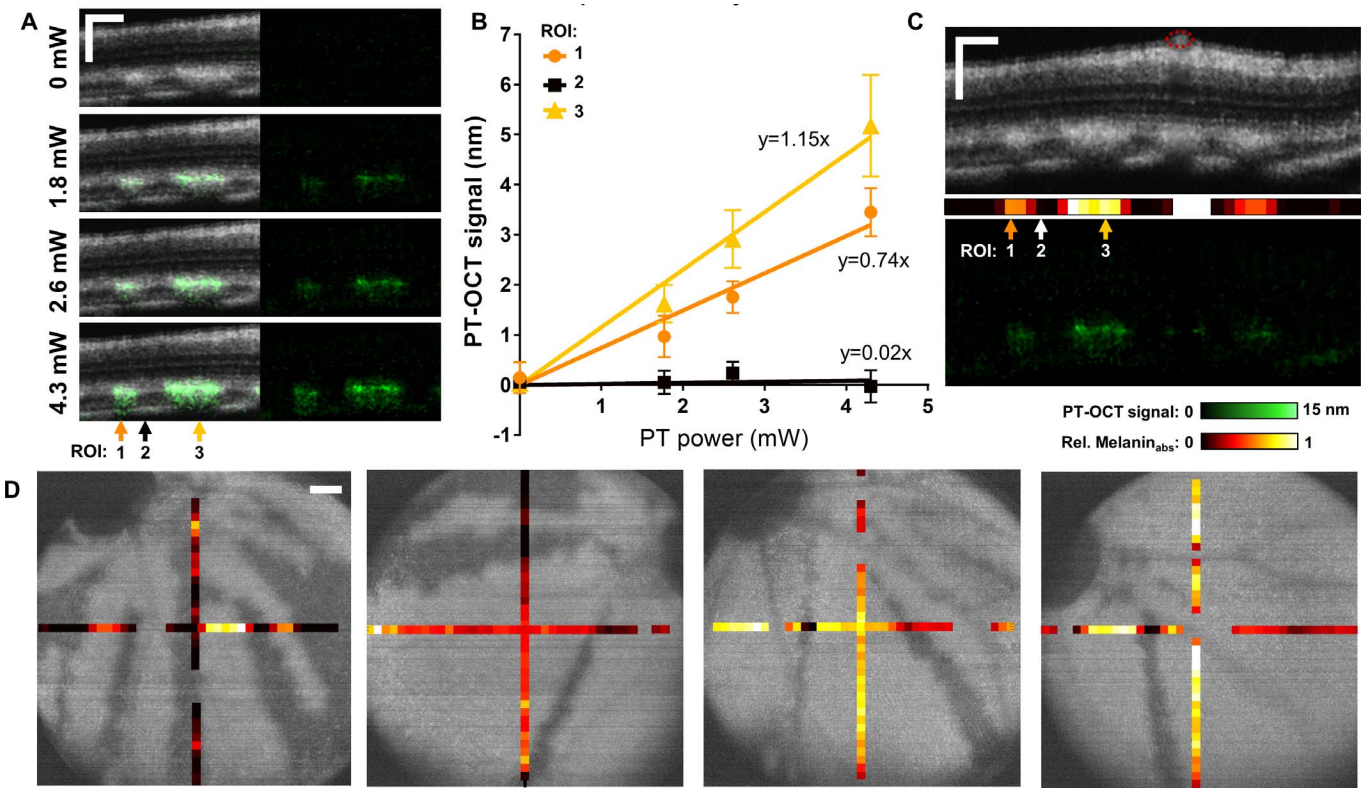

Figure 2. PT-OCT signal of melanin increases linearly with power and is indicative of melanin concentration. (A) OCT B-scans (*grayscale*, *left*) of a tyrosinase-mosaic zebrafish retina with corresponding PT-OCT signal (overlaid in *green* on the *left*, signal alone on the *right*) collected at the same location for different photothermal laser powers (0–4.3 mW). Example ROIs 1, 2, and 3 indicated by *arrows*. Each ROI is composed of 10 adjacent A-scans. (B) Average PT-OCT signal for each ROI as a function of photothermal laser power. *Error bars*: standard error across 10 adjacent A-scans. Linear fits for each ROI 1, 2, and 3 with equations $y = 0.74x$ ($R^2 = 0.96$, SSR = 0.24), $y = 0.02x$ ($R^2 = -0.35$, SSR = 0.05), and $y = 1.15x$ ($R^2 = 0.98$, SSR = 0.23), respectively. (C) OCT B-scan (*top*), melanin absorption bar corresponding to the slopes extracted in (B) (*middle*) and corresponding PT-OCT B-scan (*bottom*), with location of ROIs indicated by arrows. *Red circles* indicate blood vessels. (D) Melanin absorption bar overlaid onto en face OCT images of the RPE for four different eyes. Melanin absorption is normalized for each eye. ROIs where the PT-OCT signal did not behave as predicted by theory (slope < -0.1, $R^2 < 0.5$ and SSR > 1) are excluded for the melanin absorption (*empty space*). *Scale bar*: 100 μm.

laser is set to 1.8 mW and increases when the laser is set to higher powers (2.6 and 4.3 mW). As predicted by theory, the average PT-OCT signal increases linearly as a function of photothermal laser power for each ROI consisting of 10 averaged A-scans (Fig. 2B). Following the same model of the PT-OCT signal,[24] the slope of the linear fit should be proportional to the melanin absorption in each ROI. High melanin absorption leads to a large slope (ROI 3, Fig. 2B), while nonpigmented areas have slopes equal or almost equal to zero (ROI 2, Fig. 2B). A melanin absorption value corresponding to the slope can thus be assigned to each ROI as seen in Figure 2C. The melanin absorption values are normalized based on the highest slope obtained in each eye. ROIs where the PT-OCT signal does not increase linearly nor remain stable as a function of power ($R^2 < 0.5$ and SSR > 1, or slope < -0.1) are considered to not behave as predicted by theory, and thus no information about the melanin absorption can be inferred. These ROIs usually coincide with blood vessels, as seen in Figure 2C. Melanin absorption values are displayed for four different eyes in Figure 2D. Regions of low melanin absorption coincide with nonpigmented (dark) regions, while pigmented (light) regions have a large range of melanin absorption values. This experiment demonstrates the potential for quantitative imaging of melanin levels using PT-OCT.

PT-OCT Is Sensitive to Melanosome Translocation

To visualize the axial distribution of melanin in the retina and to characterize the effect of melanin on the

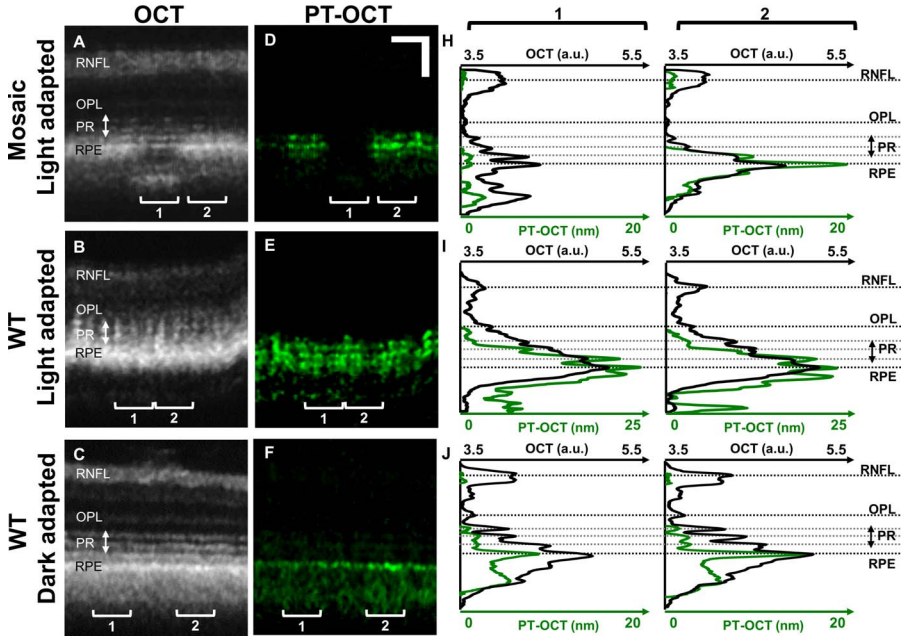

Figure 3. OCT and PT-OCT signal in the zebrafish retina as a function of depth. OCT (A–C) and PT-OCT (D–F) B-scans of light-adapted tyrosinase-mosaic zebrafish (*top*), WT light-adapted zebrafish (*middle*), and WT dark-adapted zebrafish (*bottom*) with LRP (OCT, *black*) and LAP (PT-OCT, *green*) for each ROI (H–J) 1 (*left*) and 2 (*right*). Each ROI is averaged over 20 adjacent A-scans. In (H), ROI 1 is nonpigmented, and ROI 2 is pigmented. *Scale bar*: 50 μm.

OCT signal, the PT-OCT signal as a function of depth was compared to the OCT signal at the same locations. OCT (Figs. 3A, 3B, 3C) and PT-OCT (Figs. 3D, 3E, 3F) B-scans were obtained in different zebrafish, and LRP and LAP (Figs. 3H, 3I, 3J) were computed by averaging 20 adjacent A-scans for each ROI (1 and 2). From the LAP of the tyrosinase-mosaic zebrafish in Fig. 3H (green), some low background PT-OCT signal can be seen in the nonpigmented ROI (ROI 1, left) with a strong increase in PT-OCT signal due to melanin in the pigmented region (ROI 2, right). Additionally, the central PT-OCT peak corresponds to the RPE as seen in the OCT image. There is also a second smaller PT-OCT peak at the junction between the photoreceptor layer and the RPE, and a third PT-OCT peak inside the RPE. Peaks of such intensities were not present in the nonpigmented region.

A WT light-adapted zebrafish was imaged (Figs. 3B, 3E, 3I) under the same conditions during a separate experiment, and a similar three-peak pattern can be seen in the PT-OCT signal (Fig. 3E, green), with the central peak of the LAP corresponding to the RPE and the anterior-most peak corresponding to the junction of the photoreceptors and RPE layer. This pattern was consistent and did not change with proximity to the optic nerve head.

Melanosome translocation within the RPE under different light conditions is a known phenomenon in zebrafish.[32] Under light adaptation, melanosomes should migrate to the anterior part of the RPE cells, between the individual cone outer segments, and under dark adaptation, the melanosomes should be segregated in the basal part of the RPE cells, farther away from the cones. The previous experiment was repeated on a WT zebrafish that was dark-adapted for 3 hours. Our hypothesis was that under dark adaptation, the melanosomes should be confined to the basal RPE and should not overlap with the photoreceptors. As seen in Figures 3C and 3F, the PT-OCT signal peak obtained in the dark-adapted zebrafish corresponds to the RPE. The LAP (Fig. 3J) shows a single peak without side peaks, contrary to what is seen in the light-adapted zebrafish (Figs. 3H, 3I). For this experiment, the tyrosinase-mosaic zebrafish (Figs. 3A, 3D, 3H) was imaged with 4.72 mW of photothermal laser power, while the WT light-adapted zebrafish and the WT dark-adapted zebrafish were imaged with respective powers of 2.61 and 2.85 mW; thus, the PT-OCT signal amplitude could not be compared between zebrafish for this experiment.

The melanosome translocation experiment was repeated in 10 WT light-adapted zebrafish and 11 WT dark-adapted zebrafish of the same age (Fig. 4) to

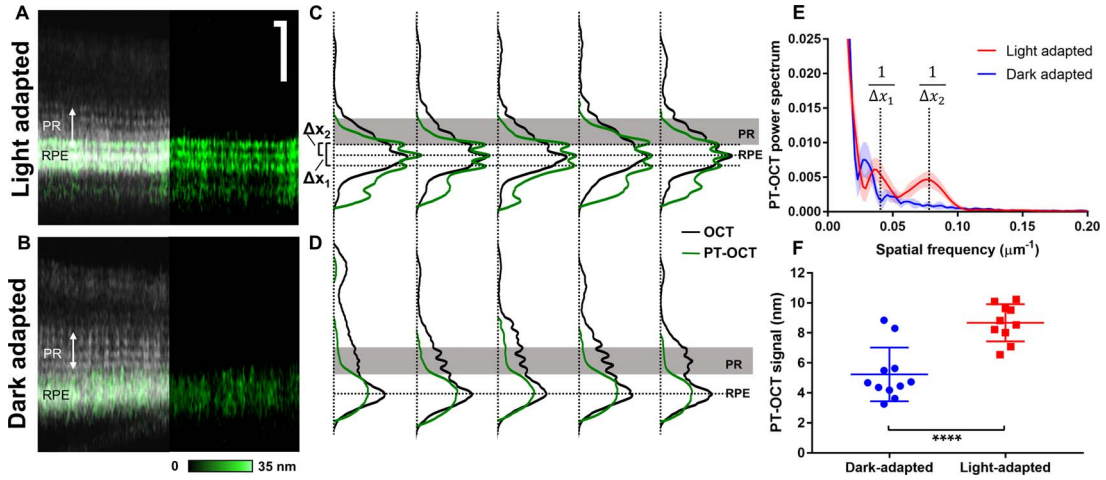

Figure 4. PT-OCT signal in light-adapted and dark-adapted WT zebrafish. (A) OCT and PT-OCT B-scan of a light-adapted and (B) dark-adapted zebrafish (PT-OCT signal overlaid in *green* onto the OCT signal on the *left*, PT-OCT alone on the *right*). *Scale bar*: 50 μm. (C) LRP (OCT, *black*) and LAP (PT-OCT, *green*) for five light-adapted zebrafish and (D) five dark-adapted zebrafish. *Horizontal dashed lines* correspond to the PT-OCT intensity peaks. *Solid gray* area indicates PR. Δx_1 and Δx_2 indicate distances between PT-OCT peaks in the light-adapted zebrafish. (E) PT-OCT power spectrum obtained from the 10 light-adapted (*red*) and 11 dark-adapted (*blue*) zebrafish. *Solid line*: mean; *shaded region*: standard deviation. The spatial frequencies corresponding to $1/\Delta x_1$ and $1/\Delta x_2$ are indicated. (F) Average PT-OCT signal per eye for all dark-adapted (*blue*) and light-adapted zebrafish (*red*). *Error bars*: standard deviation. ****$P < 0.0001$ Student's *t*-test.

confirm the results seen in the preliminary data (Fig. 3). All zebrafish were imaged on the same day with the same photothermal laser power (2.07 mW). The light-adapted zebrafish reliably display a three-band pattern (Fig. 4A) seen in previous experiments, while the dark-adapted zebrafish do not have such pattern (Fig. 4B). LRPs and LAPs were created by averaging the entire OCT and PT-OCT B-scan (400 A-scans) for each zebrafish (Fig. 4C, 4D). B-scans without major blood vessels were chosen in each eye to optimize phase stability and the PT-OCT signal quality over the entire B-scan. As seen previously, three peaks are seen in the PT-OCT signal for all light-adapted zebrafish (see five example zebrafish in Fig. 4C), where the central peak corresponds to the RPE and the anterior-most peak overlaps with a photoreceptor band. This pattern was not seen in any of the dark-adapted zebrafish (see five examples in Fig. 4D) where the PT-OCT signal is limited to the RPE and is composed of a single peak. A Fourier transform of the LAPs seen in Figures 4C and 4D was performed to analyze the spatial frequency distribution (Fig. 4E) for all 21 zebrafish. Two regions of spatial frequency are significantly different between the light-adapted group and the dark-adapted group, which correspond to the distance between the anterior-most and posterior-most absorption bands ($\Delta x_1 = 23.6$ μm) and between the anterior-most and middle bands ($\Delta x_2 = 11.8$ μm) in light-adapted zebrafish (Fig. 4E). This spatial frequency analysis quantitatively highlights the differences in PT-OCT depth profiles between the light- and dark-adapted groups ($P = 0.0001$ at $1/\Delta x_1$ and $P < 0.0001$ at $1/\Delta x_2$, Student's *t*-test). Additionally, the average PT-OCT signal intensity per B-scan was calculated for both experimental groups (Fig. 4F). A significantly higher PT-OCT signal was detected in the light-adapted group compared to the dark-adapted group ($P < 0.0001$, Student's *t*-test), which indicates higher melanin absorption in light-adapted zebrafish.

Histology was performed on the zebrafish eyes to confirm melanosome translocation between the light- and dark-adapted groups. Example OCT B-scans can be seen in Figure 5A for the light-adapted zebrafish and Figure 5B for the dark-adapted zebrafish, with corresponding PT-OCT B-scans in Figures 5C and 5D. As seen previously, the three-band pattern is present in the PT-OCT image of the light-adapted zebrafish (Fig. 5C), but not in the dark-adapted zebrafish (Fig. 5D). Histology was performed on the same zebrafish after imaging, and the corresponding histology sections are shown in Figues 5E and 5F. As expected, the melanosomes in the light-adapted zebrafish have accumulated in the anterior part of the RPE cells and are surrounding the outer segments of the photoreceptors (Fig. 5E, OS). There are almost no melanosomes left in the posterior part of the RPE cells, where nuclei are visible. In comparison, the

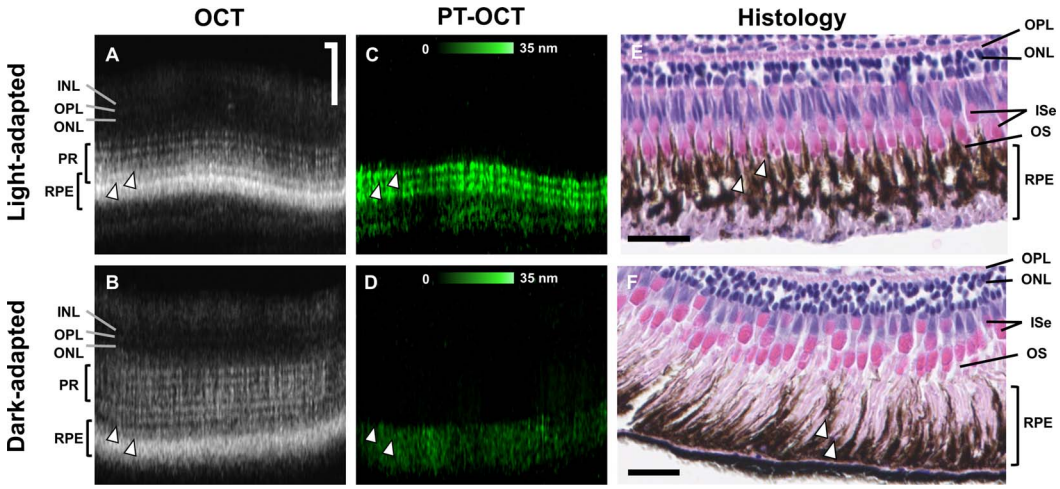

Figure 5. Melanosome migration observed in histology sections. (A, B) OCT and (C, D) corresponding PT-OCT B-scans with (E, F) corresponding H&E histology sections from the same animal for both light-adapted (A, C, E) and dark-adapted (B, D, F) zebrafish. *White arrowheads* indicate different structures where melanin is present (coregistered between images A and C, and B and D, approximate location for images E and F). *Scale bar*: 50 μm for OCT and PT-OCT images, 25 μm for histology. INL, inner nuclear layer; ISe, photoreceptor inner segment ellipsoid zone; OS, photoreceptor outer segment.

melanosomes in the dark-adapted zebrafish have migrated to the basal part of the RPE cells, farther away from the photoreceptors (Fig. 5F), which is expected in dark-adapted zebrafish.[32] These results confirm that melanosome translocation occurred as previously documented and that our light-adapted group and dark-adapted group have different melanin distributions within the RPE. From this study, we conclude that PT-OCT is sensitive to differences in melanin distribution and absorption between light- and dark-adapted zebrafish.

Discussion

PT-OCT is a functional OCT technique that detects optical absorbers such as gold nanoparticles[25] or indocyanine green[35] and has recently been demonstrated in the eye for the first time.[28] In this study, we used PT-OCT to image the distribution of melanin in the zebrafish retina. Melanin is naturally present in the RPE, and changes in retinal pigmentation are observed in multiple eye conditions, such as AMD,[6] albinism,[36] and retinitis pigmentosa.[37] PT-OCT could provide a valuable imaging technique to quantify the distribution of melanin in the retina across different patients/diseases.

For this experiment, we first validated that the PT-OCT signal was specific to melanin by imaging tyrosinase-mosaic zebrafish. In the past, PT-OCT of melanin in the eye had only been tested by comparing WT mice to albino mice imaged during separate experiments.[28] Thus, the current study provided a more robust validation of PT-OCT sensitivity to melanin within a single retina. We further demonstrated that the PT-OCT signal for pigmented ROIs increases linearly with laser power, as predicted by theory. Thus, the high variance in PT-OCT signal over all pigmented ROIs does not appear to be the result of a high uncertainty on the measurements, but likely a large range of absorption coefficients throughout the retina. This result indicates that PT-OCT could be used to quantify changes in melanin concentration within the eye.

Next, we characterized changes in melanin distribution as a function of depth within the retina. The most noticeable feature observed in the PT-OCT signal is the three-band pattern that was reliably seen in light-adapted zebrafish across different experiments, zebrafish cohorts (WT and tyrosinase-mosaic), and photothermal laser powers. This three-band pattern was never seen in dark-adapted fish. We also detected an increase in PT-OCT signal intensity in the light-adapted zebrafish group compared to the dark-adapted group, even though dark adaptation alone is unlikely to cause changes in total melanin amounts and both groups were imaged at the same time of the day.[38] In the zebrafish, light-based melanosome migration is thought to control the exposure of the photoreceptors to incoming light.[32] During light adaptation, melanosomes surround the photoreceptors to absorb some of the excessive incoming light and reduce bleaching, while during dark adaptation

the opposite situation takes place, and melanosomes migrate away from the photoreceptors to maximize their exposure to light. The same behavior was seen in our PT-OCT measurements: during light adaptation, more light was absorbed by the melanin and converted into heat, which increased the PT-OCT signal, while during dark adaptation, more light was absorbed by the photoreceptors and less melanin absorption occurred from the remaining light, leading to a decrease in the PT-OCT signal. However, it is not known if aggregation of melanosomes could also affect the absorption properties of melanin and change the PT-OCT signal between the light-adapted and dark-adapted groups. A similar study by Zhang et al.[9] used OCT to observe melanosome translocation in the RPE of frogs and observed an increase in OCT intensity with dark adaptation. This was due to the aggregation of the highly scattering melanosomes in the apical part of the RPE cells. This demonstrates that PT-OCT measurements provide complementary information to OCT by using a different contrast mechanism. Overall, both the changes in PT-OCT signal appearance and intensity indicate that PT-OCT is sensitive to intracellular changes in pigmentation. In the future, PT-OCT could be used to examine other models of retinal disease involving changes in pigmentation.[39]

Comparing the OCT/PT-OCT signal to histology could lead to a better understanding of the anatomical features that lead to specific bands in the OCT signal. For example, in animal models with retinomotor movements, researchers could compare histology to the OCT and PT-OCT signal to better determine the origin of the outer retinal bands. In this study, the histology section of the light-adapted zebrafish shows some cone outer segments surrounded by melanin (Fig. 4E). In the corresponding OCT/PT-OCT image, the anterior-most band of the three-band PT-OCT pattern overlaps with one of the OCT photoreceptor bands, which could help localize the origin of the OCT bands. In comparison, the melanosomes in the dark-adapted zebrafish are segregated in the basal outer part of the RPE cells and do not overlap with any photoreceptors, which results in an absence of band-like features in the PT-OCT signal.

There are, however, limitations to this study. More comparative anatomy is needed before findings from the zebrafish can be generalized to humans. Additionally, shadowing and phase accumulation are two artifacts present in the PT-OCT signal[40,41] that will affect the signal intensity as a function of depth. For this reason, it is difficult to precisely quantify the distribution of melanin as a function of depth, and artifacts can be seen on some images (such as Fig. 3F where significant shadowing is seen below the RPE). In terms of experimental parameters, the photothermal laser power will have to be reduced in future studies to comply with American National Standards Institute (approximately 0.5 mW maximum permissible exposure at $\lambda = 685$ nm, compared to 1.8 mW used in this study). To translate this technique to human retinal imaging, scanning times will also have to be reduced, which could be accomplished by reducing the number of repeated A-scans acquired for each pixel and increasing the amplitude-modulation frequency of the photothermal laser.

In summary, we have demonstrated PT-OCT in the zebrafish eye, we believe for the first time. We have validated that the PT-OCT signal is specific to melanin. We have characterized changes in the PT-OCT signal based on light-driven melanosome translocation within RPE cells. Additionally, we have compared PT-OCT images to histology sections, which inform how different features of the OCT signal are interpreted. PT-OCT could be applied to the wide array of zebrafish models and other models of retinal diseases to facilitate mechanistic studies or identify early diagnostic features of diseases. In addition, PT-OCT could be used to monitor response to drugs that aim to correct defective melanin biosynthesis.

Acknowledgments

The authors thank Suresh Kumar, Samantha Servi, and Christine Duris for their assistance with this study, and Barbara Blodi for helpful discussions.

Supported in part by the National Center for Advancing Translational Sciences of the National Institutes of Health (NIH) under award numbers UL1TR001436 and TL1TR001437; by the National Eye Institute of the NIH under award numbers R01EY016060, P30EY001931, and F30EY0277706; and by the National Institute of General Medical Sciences of the NIH under award number T32GM080202. The content is solely the responsibility of the authors and does not necessarily represent the official views of the National Institutes of Health. Additional support came from the Alcon Research Institute and the Foundation Fighting Blindness (PPA-0617-0718).

Disclosure: **M. Lapierre-Landry**, None; **A.L. Huck-**

enpahler, None; **B.A. Link**, None; **R.F. Collery**, None; **J. Carroll**, None; **M.C. Skala**, None

References

1. Fujimoto J, Swanson E. The development, commercialization, and impact of optical coherence tomography. *Invest Ophthalmol Vis Sci*. 2016;57:OCT1–OCT13.
2. Staurenghi G, Sadda S, Chakravarthy U, Spaide RF. Proposed lexicon for anatomic landmarks in normal posterior segment spectral-domain optical coherence tomography: the IN• OCT consensus. *Ophthalmology*. 2014;121:1572–1578.
3. Anger EM, Unterhuber A, Hermann B, et al. Ultrahigh resolution optical coherence tomography of the monkey fovea. Identification of retinal sublayers by correlation with semithin histology sections. *Exp Eye Res*. 2004;78:1117–1125.
4. Spaide RF, Curcio CA. Anatomical correlates to the bands seen in the outer retina by optical coherence tomography: literature review and model. *Retina*. 2011;31:1609.
5. Jonnal RS, Kocaoglu OP, Zawadzki RJ, Lee S-H, Werner JS, Miller DT. The cellular origins of the outer retinal bands in optical coherence tomography images. *Invest Ophthalmol Vis Sci*. 2014;55:7904–7918.
6. Bhutto I, Lutty G. Understanding age-related macular degeneration (AMD): relationships between the photoreceptor/retinal pigment epithelium/Bruch's membrane/choriocapillaris complex. *Mol Aspects Med*. 2012;33:295–317.
7. Kellner U, Kellner S, Weber BH, Fiebig B, Weinitz S, Ruether K. Lipofuscin- and melanin-related fundus autofluorescence visualize different retinal pigment epithelial alterations in patients with retinitis pigmentosa. *Eye*. 2009;23:1349.
8. Klein ML, Ferris FL, Armstrong J, et al. Retinal precursors and the development of geographic atrophy in age-related macular degeneration. *Ophthalmology*. 2008;115:1026–1031.
9. Zhang Q-X, Lu R-W, Messinger JD, Curcio CA, Guarcello V, Yao X-C. In vivo optical coherence tomography of light-driven melanosome translocation in retinal pigment epithelium. *Sci Rep*. 2013;3.
10. Wilk MA, Huckenpahler AL, Collery RF, Link BA, Carroll J. The effect of retinal melanin on optical coherence tomography images. *Trans Vis Sci Tech*. 2017;6:8–8.
11. Keilhauer CN, Delori FoC. Near-infrared autofluorescence imaging of the fundus: visualization of ocular melanin. 2006;47:3556–3564.
12. Duncker T, Tabacaru MR, Lee W, Tsang SH, Sparrow JR, Greenstein VC. Comparison of near-infrared and short-wavelength autofluorescence in retinitis pigmentosa. *Invest Ophthalmol Vis Sci*. 2013;54:585–591.
13. Yoshitake S, Murakami T, Horii T, et al. Qualitative and quantitative characteristics of near-infrared autofluorescence in diabetic macular edema. *Ophthalmology*. 2014;121:1036–1044.
14. Zhang X, Puliafito CA, Jiao S, Zhang HF. Simultaneous in vivo imaging of melanin and lipofuscin in the retina with photoacoustic ophthalmoscopy and autofluorescence imaging. *J Biomed Opt*. 2011;16:080504.
15. Shu X, Li H, Dong B, Sun C, Zhang HF. Quantifying melanin concentration in retinal pigment epithelium using broadband photoacoustic microscopy. *Biomed Opt Express*. 2017;8:2851–2865.
16. De Boer JF, Milner TE, van Gemert MJ, Nelson JS. Two-dimensional birefringence imaging in biological tissue by polarization-sensitive optical coherence tomography. *Opt Lett*. 1997;22:934–936.
17. Adler DC, Huang SW, Huber R, Fujimoto JG. Photothermal detection of gold nanoparticles using phase-sensitive optical coherence tomography. *Opt Express*. 2008;16:4376–4393.
18. Skala MC, Crow MJ, Wax A, Izatt JA. Photothermal optical coherence tomography of epidermal growth factor receptor in live cells using immunotargeted gold nanospheres. *Nano Lett*. 2008;8:3461–3467.
19. Pircher M, Hitzenberger CK, Schmidt-Erfurth U. Polarization sensitive optical coherence tomography in the human eye. *Prog Retin Eye Res*. 2011;30:431–451.
20. Baumann B, Schirmer J, Rauscher S, et al. Melanin pigmentation in rat eyes: in vivo imaging by polarization-sensitive optical coherence tomography and comparison to histology. *Invest Ophthalmol Vis Sci*. 2015;56:7462–7472.
21. Götzinger E, Pircher M, Geitzenauer W, et al. Retinal pigment epithelium segmentation by polarization sensitive optical coherence tomography. *Opt Express*. 2008;16:16410–16422.
22. Baumann B. Polarization sensitive optical coherence tomography of melanin provides intrinsic contrast based on depolarization. *Biomed Opt Express*. 2012;3:1670–1683.

23. Zhou C, Tsai T-H, Adler DC, et al. Photothermal optical coherence tomography in ex vivo human breast tissues using gold nanoshells. *Opt Lett*. 2010;35:700–702.
24. Tucker-Schwartz J, Meyer T, Patil C, Duvall C, Skala M. In vivo photothermal optical coherence tomography of gold nanorod contrast agents. *Biomed Opt Express*. 2012;3:2881–2895.
25. Jung Y, Reif R, Zeng Y, Wang RK. Three-dimensional high-resolution imaging of gold nanorods uptake in sentinel lymph nodes. *Nano Lett*. 2011;11:2938–2943.
26. Subhash HM, Xie H, Smith JW, McCarty OJ. Optical detection of indocyanine green encapsulated biocompatible poly (lactic-co-glycolic) acid nanoparticles with photothermal optical coherence tomography. *Opt Lett*. 2012;37:981–983.
27. Makita S, Yasuno Y. In vivo photothermal optical coherence tomography for non-invasive imaging of endogenous absorption agents. *Biomed Opt Express*. 2015;6:1707–1725.
28. Lapierre-Landry M, Gordon AY, Penn JS, Skala MC. In vivo photothermal optical coherence tomography of endogenous and exogenous contrast agents in the eye. *Sci Rep*. 2017;7:9228.
29. Huckenpahler AL, Wilk MA, Cooper RF, et al. Imaging the adult zebrafish cone mosaic using optical coherence tomography. *Vis Neurosci*. 2016;33.
30. Bailey TJ, Davis DH, Vance JE, Hyde DR. Spectral-domain optical coherence tomography as a noninvasive method to assess damaged and regenerating adult zebrafish retinas. *Invest Ophthalmol Vis Sci*. 2012;53:3126–3138.
31. Howe DG, Bradford YM, Eagle A, et al. The zebrafish model organism database: new support for human disease models, mutation details, gene expression phenotypes and searching. *Nucleic Acids Res*. 2016;45:D758–D768.
32. Hodel C, Neuhauss SC, Biehlmaier O. Time course and development of light adaptation processes in the outer zebrafish retina. *Anat Rec*. 2006;288:653–662.
33. Wojtkowski M, Srinivasan VJ, Ko TH, Fujimoto JG, Kowalczyk A, Duker JS. Ultrahigh-resolution, high-speed, Fourier domain optical coherence tomography and methods for dispersion compensation. *Opt Express*. 2004;12:2404–2422.
34. Guizar-Sicairos M, Thurman ST, Fienup JR. Efficient subpixel image registration algorithms. *Opt Lett*. 2008;33:156–158.
35. Tucker-Schwartz JM, Lapierre-Landry M, Patil CA, Skala MC. Photothermal optical lock-in optical coherence tomography for in vivo imaging. *Biomed Opt Express*. 2015;6:2268–2282.
36. Summers CG. Albinism: classification, clinical characteristics, and recent findings. *Optom Vis Sci*. 2009;86:659–662.
37. Fahim AT, Daiger SP, Weleber RG. Nonsyndromic retinitis pigmentosa overview. In: Adam MP, Ardinger HH, Pagon RA, et al., eds. *GeneReviews*. Seattle, WA: University of Washington; 2000:1993–2018.
38. Li Y, Li G, Wang H, Du J, Yan J. Analysis of a gene regulatory cascade mediating circadian rhythm in zebrafish. *PLoS Comput Biol*. 2013;9:e1002940.
39. Link BA, Collery RF. Zebrafish models of retinal disease. *Annu Rev Vis Sci*. 2015;1:125–153.
40. Lapierre-Landry M, Tucker-Schwartz JM, Skala MC. Depth-resolved analytical model and correction algorithm for photothermal optical coherence tomography. *Biomed Opt Express*. 2016;7:2607–2622.
41. Guan G, Reif R, Huang Z, Wang RK. Depth profiling of photothermal compound concentrations using phase sensitive optical coherence tomography. *J Biomed Opt*. 2011;16:126003–1260039.